analytical chemistry

pubs.acs.org/ac Article

Poly-L-Lysine-Modified Graphene Field-Effect Transistor Biosensors for Ultrasensitive Breast Cancer miRNAs and SARS-CoV-2 RNA Detection

Jianwei Gao, Chunhua Wang, Chao Wang, Yujin Chu, Shun Wang, Ming yuan Sun, Hao Ji, Yakun Gao, Yanhao Wang, Yingkuan Han, Fangteng Song, Hong Liu, Yu Zhang,* and Lin Han*

Cite This: *Anal. Chem.* 2022, 94, 1626−1636 Read Online

ACCESS | Metrics & More | Article Recommendations | Supporting Information

ABSTRACT: (Mi)RNAs are important biomarkers for cancers diagnosis and pandemic diseases, which require fast, ultrasensitive, and economical detection strategies to quantitatively detect exact (mi)RNAs expression levels. The novel coronavirus disease (SARS-CoV-2) has been breaking out globally, and RNA detection is the most effective way to identify the SARS-CoV-2 virus. Here, we developed an ultrasensitive poly-L-lysine (PLL)-functionalized graphene field-effect transistor (PGFET) biosensor for breast cancer miRNAs and viral RNA detection. PLL is functionalized on the channel surface of GFET to immobilize DNA probes by the electrostatic force. The results show that PGFET biosensors can achieve a (mi)RNA detection range of five orders with a detection limit of 1 fM and an entire detection time within 20 min using 2 μL of human serum and throat swab samples, which exhibits more than 113% enhancement in terms of sensitivity compared to that of GFET biosensors. The performance enhancement mechanisms of PGFET biosensors were comprehensively studied based on an electrical biosensor theoretical model and experimental results. In addition, the PGFET biosensor was applied for the breast cancer miRNA detection in actual serum samples and SARS-CoV-2 RNA detection in throat swab samples, providing a promising approach for rapid cancer diagnosis and virus screening.

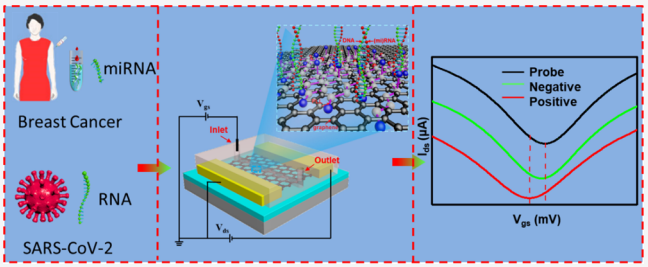

INTRODUCTION

Cancers are the biggest threat for human health in the world, in which breast cancer ranks the top for women. Recently, another newly emerged coronavirus (SARS-CoV-2) that can cause viral pneumonia has spread globally and is threatening the global public health. To effectively control its prevalence, rapid and accurate detection of RNAs or miRNAs, a class of single-stranded nucleic acid molecules encoded by endogenous genes and involved in the regulation of post-transcriptional gene expression,[1−3] becomes a critical requirement. It has been demonstrated that different (mi)RNAs and their expression levels are associated with various diseases.[4−7] Real-time reverse transcription polymerase chain reaction is the popular commercial nucleic acid test tool and the only officially proved specific determination method of SARS-CoV-2 RNA, but it is time-consuming. Therefore, developing a sensitive, selective, rapid, and low-cost (mi)RNA detection method is of great significance for clinical diagnosis and virus detection.[8−11]

Graphene, an atom-thick 2D carbon material, was used in biosensing applications because of its excellent physical and chemical properties, such as high intrinsic carrier mobility, direct interaction with molecules, large surface areas, and low intrinsic noise.[12−14] Together with the FET biosensor advantages of being label-free, fast, sensitive, selective, and low cost and possessing on-site detection and a small sample volume consumption,[15−17] the graphene-based field-effect transistor (GFET) biosensor has been paid attractive attention for cancer diagnosis and virus screening.[18−21] Previously, direction immobilization of DNA probes on a GFET channel surface for sensitive nucleic acid detection was reported by our group[22] and others.[23−25] The limit of detection of 10 fM for miRNAs was achieved;[22] however, it still needs to be improved further to fulfil the actual requirements. To improve the performance of GFET biosensors, channel surface functionalization of GFET becomes crucial. Different strategies were reported to understand the sensing mechanisms and improve the sensing performances,[26,27] such as Au nanoparticles (AuNPs), 1-pyrenebutyric acid succinimidyl ester (PBASE), and so on.[23,28] Cai et al. developed a graphene FET biosensor functionalized with AuNPs for the label-free detection of miRNAs, which improved the detection limit to 1 fM.[27] Xu et al. demonstrated that PBASE-decorated GFET biosensors

Received: September 1, 2021
Accepted: January 4, 2022
Published: January 13, 2022

https://doi.org/10.1021/acs.analchem.1c03786
Anal. Chem. 2022, 94, 1626−1636

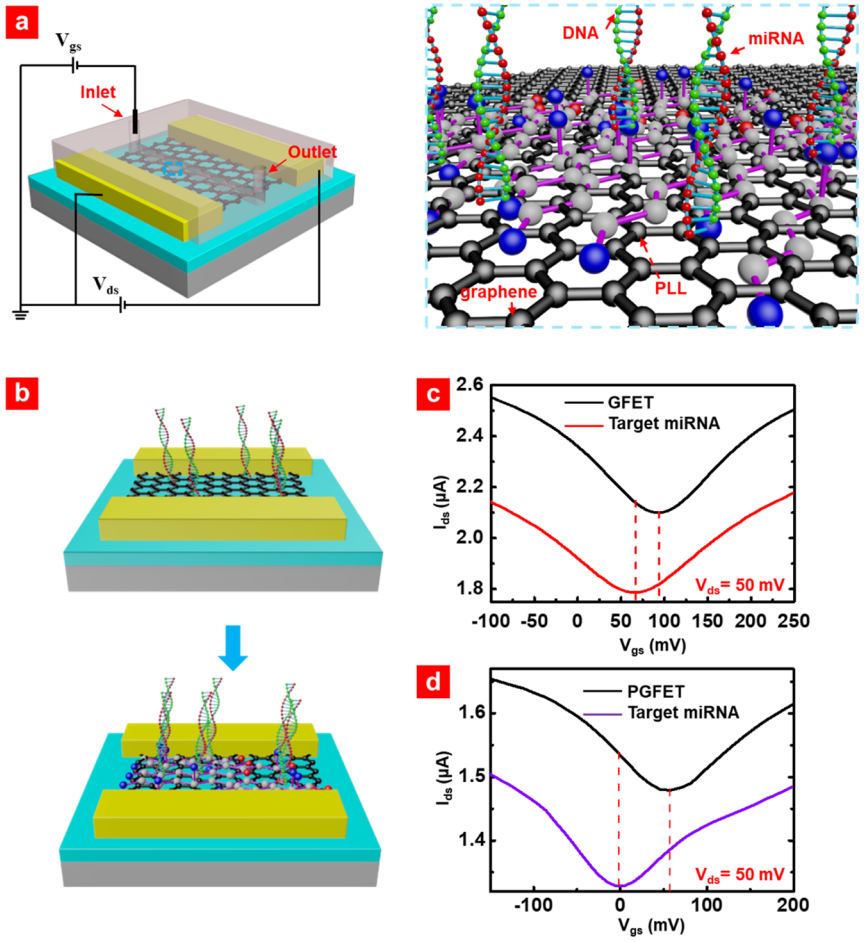

Figure 1. (a) PGFET biosensor Schematic. (b) Schematic principles of GFET and PGFET for miRNA detection. Comparison of miRNA detection results between GFET (c) and PGFET(d) biosensor.

could reliably monitor the kinetics of nucleic acid binding and unbinding by recording electrical signals in real time, and it showed the limit of detection of 0.25 nM.[25] Recently, Seo et al. also used PBASE as a linker to construct GFET biosensors for COVID-19 virus detection.[29] Among those reports, the GFET functionalization process was suffering from either instability or time consumption issues. Therefore, a simple and stable functionalization approach to construct GFET biosensors is essential. Poly-L-lysine (PLL) is rich in cations and has a strong electrostatic force with substances with anions. It is an important material for biomolecular detection with fluorescence signals and is widely used in the field of biomedicine.[30−33] PLL exhibits several advantages during biosensing, including its easy interaction with not only nucleic acids and proteins but also with graphene, short process time of less than 20 min. However, there is no any report using PLL to combine it with electronic devices for the biosensing applications.

In this work, we developed a new multi-functional graphene FET with a PLL-functionalized channel (PGFET) biosensor integrated with a microfluidic structure, in short a PGFET biosensor, for ultrasensitive, specific, rapid detection of breast cancer miRNAs and SARS-CoV-2 RNAs, as shown in Figure 1. This is the first proof of concept of breast cancer miRNA and SARS-CoV-2 RNA detection using a PGFET biosensor, which achieves a detection limit of 1fM within 20 min using 2 μL samples, and wide dynamic detection of five orders magnitudes. The performance enhancement mechanism of PGFET biosensors was studied based on electrical sensing model and experimental results. The detection of breast cancer serum samples and simulated SARS-CoV-2 samples demonstrated their practical application capabilities.

EXPERIMENTAL SECTION

Materials. Phosphate buffered saline (PBS) was bought from Corning. FAM-labeled DNA probes and miRNAs were synthesized and ordered from Takara Biotechnology Co. Ltd. The 0.01% PLL solution and ethanolamine (EA) were purchased from Sigma-Aldrich. Monolayer graphene was grown by CVD.[34]

Fabrication of PGFET Biosensors. The detailed manufacturing process of PGFET biosensors is shown in Figure S1a−g. A single layer of graphene on a copper foil was protected by a polymethyl methacrylate (PMMA) thin layer. The copper foil was etched away by 0.1 M ferric chloride solution. The graphene/PMMA was transferred onto a 200 × 200 mm^2 Si/SiO_2 substrate, and finally, the PMMA layer was stripped off in acetone for 90 min. The source and drain electrodes of 10 nm/50 nm Ti/Au were deposited by electron beam evaporation deposition.[35,36] The microfluidic channel was fabricated[37,38] and integrated with the PGFETs under optical microscopy. The size of the PDMS chip was 9 mm × 9 mm × 1 mm with a channel of 6000 μm × 250 μm × 40 μm. Ag/AgCl reference electrodes were used as a gate electrode in PBS solutions. The PGFET biosensor schematic is shown in

https://doi.org/10.1021/acs.analchem.1c03786
Anal. Chem. 2022, 94, 1626−1636

Table 1. NDA and RNA Sequences

annotation		sequence (5′ to 3′)
DNA probes	P-4732	ACATCTCGTCCCTCGTCCTTCGA
	P-191	CAGCTGCTTTTGGGATTCCGTTG
	P-125	TCACAAGTTAGGGTCTCAGGGA
	P-21	TCAACATCAGTCTGATAAGCTA
	P-SARS-CoV-2	GTGAAATGGTCATGTGTGGCGGTTC
		ACTATATGTTAAACCAGGTGGAAC
(mi)RNA	miR-4732	AAAAGGCGGGAGAAGCCCCA
	miR-191	CAACGGAAUCCCAAAAGCAGCUG
	miR-125	UCCCUGAGACCCUAACUUGUGA
	miR-21	UAGCUUAUCAGACUGAUGUUGA
	T-SARS-CoV-2 RNA	GUUCCACCUGGUUUAACAUAUAGUG
		AACCGCCACACAUGACCAUUUCAC
	mis-SARS-CoV-2 RNA	GUUCCACCUGGUUUAACAUAUAG
		UAAACCGCCACACAUGACCAUUUCAC
	non-SARS-CoV-2 RNA	AAGAAUACCACGAAAGCAAGAAAAAGAA
		GUACGCUAUUAACUAUUAACGUACCUGU

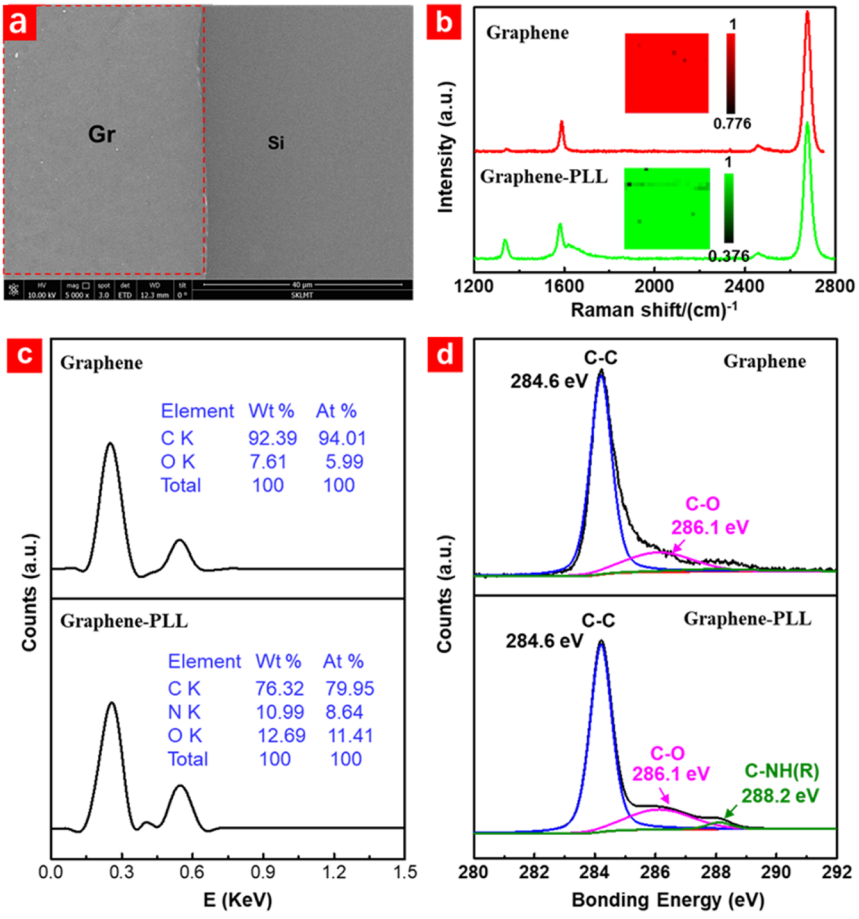

Figure 2. (a) SEM images of graphene on silicon substrate. (b) Raman spectra of transferred monolayer graphene without (red) and with (green) PLL-modification. (c) EDS of graphene (upper) and PLL−graphene (lower). (d) XPS spectra of graphene (upper) and PLL−graphene (lower).

Figure 1a. 1 mg/mL PLL was used to functionalize the graphene channel to immobilize DNA probes. First, PLL was loaded into the microfluidic channel for 1 h at room temperature, then the channel was rinsed. DNA probe solution of 10 μM was pumped into the gate channel and reacted with the channel surface for 1 h followed by rinsing with 1× PBS to flush away the extra unreacted DNA probes. Finally, the PGFETE was blocked with 100 mM EA for 30 min to avoid possible nonspecific adsorption on the graphene surface followed by rinsing with 1× PBS. The PGFET biosensor is ready for RNA detection.

(mi)RNA Detection. The miRNA detection could be performed via monitoring the V_{dirac} shift of the devices after DNA−miRNA hybridization in the channel. DNA−(mi)RNA reaction was performed by loading certain concentration of target (mi)RNAs into the biosensor channel with incubation

https://doi.org/10.1021/acs.analchem.1c03786
Anal. Chem. 2022, 94, 1626−1636

for 10 min. After that, the microfluidic channel was flushed by 1× PBS. The $I_{ds}-V_{gs}$ curves were measured on the probe station using a Keithley 2636B source meter. The DNA and (mi)RNA sequences used in this work are presented in Table 1. Schematic principles of GFET and PGFET for miRNA detection are shown in Figure 1b. Compared to the GFET biosensor, PGFET biosensors can give a more obvious Dirac point shift, so the sensitivity of miRNA detection can be improved (Figure 1c,d).

Characterizations. Scanning electron microscopy (SEM) was characterized by ZEISS Sigma 500. Energy dispersive X-ray spectroscopy (EDS) was measured on a 2000XMS instrument (EDAX, Inc). Atomic force microscopy (AFM) images were obtained using a Dimension 3100 (Veeco, CA) in non-contact mode. The Raman spectrometer (Renishaw, UK) was used for the Raman spectra measurement with a 1.5 mW 532 nm laser excitation and an exposure time of 10 s. X-ray photoelectron spectroscopy (XPS) measurement was conducted on a Kratos machine (AXIS Supra).

RESULTS AND DISCUSSION

Characterization of PGFET. The optical photo of the PGFET is shown in Figure S2a, where a single-layer graphene crosses the source and drain electrodes forming a FET channel (the red dashed line labeled area). Figure 2a shows the SEM images of the graphene transferred onto a silicon substrate, which presents a clean graphene and smooth surface. AFM images of the graphene area with (right) and without (left) PLL modification (Figure S2b) further confirmed the above observation, which presents the RMS surface roughness of 1.92 and 2.87 nm for graphene and PLL−graphene, respectively. To further evaluate the graphene and PLL−graphene, the Raman spectra of monolayer graphene before and after PLL-functionalization were characterized (Figure 2b). It indicated that transferred graphene is a high-quality monolayer film based on the 2D peak to a G peak ratio of 3.26.[39] The graphene Raman mapping on 20 × 20 μm^2 area (the inset of Figure 2b) proved the larger area uniformity of the transferred graphene. After PLL modification, the characteristic peaks of PLL (1306 and 1667 cm^{-1}) are clearly observed in Figure 2b (green line), and the typical Raman spectrum of PLL is shown in Figure S3. The heating map indicates that PLL was uniformly distributed on the graphene surface. The PLL functionalization of the graphene surface has also been confirmed further by EDS. The molar ratio of O to C increases from 0.0599 of graphene to 0.1141 of graphene-PLL, and nitrogen is present (8.64 At %) in the PLL−graphene characterized by EDS (Figure 2c). To further evaluate the quality and interaction between graphene, PLL, and DNA probes, we performed the TEM of the samples as shown in Figure S4. It shows that the graphene is a single crystalline solid(Figure S4a−c). After PLL functionalization and DNA probe immobilization, the graphene lattice structure gradually blurred (Figure S4d−f). The EDX images of graphene (Figure S4g), PLL/graphene (Figure S4h), and DNA probe/PLL/graphene (Figure S4i) confirmed the successful binding of PLL and DNA probe because of the presence of N and O elements for PLL (Figure S4h) and N, O, and P elements for DNA probes (Figure S4i). In addition, XPS also confirmed the PLL functionalization on the graphene surface. There is an additional absorption peak at 288.2 eV, which corresponds to the carbon in the C−N bonds, as shown in Figure 2d. These results fully proved that graphene has been functionalized with PLL successfully.

The electrical characteristics (output and transfer curves) of the PGFET were evaluated after PLL functionalization on graphene. Under a constant V_{gs}, I_{ds} and V_{ds} are linear (Figure S5a). After PLL functionalization on the graphene surface, the device resistance increases, which is due to the covalent bond interaction between PLL and graphene. The typical ambipolar behavior of PGFET is also observed, which is consistent with the reported graphene FETs.[40] The Dirac point V_{dirac} is shifted to the left ∼21 mV after PLL functionalization on a channel graphene surface of the device (Figure S5b−c). The left shift of V_{dirac} is due to the n-doping of the graphene by the negatively charged PLL.[41] Because the PGFET biosensor sensing process is carried out in a solution environment, the stability of PGFET is a very important factor. Based on our previous work, the GFET presented good stability at least for four months.[42] In Figure S5b,c, it is shown that the V_{Daric} only presents a slight change within 72 h. The stability of the PGFET device is much more stable than that of GFET devices, which are 5 and 11 mV for PGFET and GFET, respectively. The V_{dirac} variation of the PGFET and GFET may be caused by ion adsorption in PBS solution, and a slight variation in practical application is acceptable.[43−45]

To demonstrate the successful fabrication of PGFET and GFET biosensors, the transfer curves of the biosensors were performed in each step, including before and after PLL functionalization, DNA probes immobilization, and DNA-target miRNA incubation. The V_{dirac} of the PGFET biosensor shifted to left about 31 mV after PLL functionalization (Figure S6) due to negative charged PLL induced n-doping of the graphene, which is similar to the PBASE-modified graphene FET biosensors.[25] Further left shift of 39 mV was obtained after DNA probe immobilization on the PLL, and ∼46 mV left shift after 10 pM target miRNA incubation. GFET biosensors showed a similar trend but small V_{dirac} shift values. These results confirmed the successful construction of PGFET and GFET biosensors, and essential improvement of the biosensor performance through PLL functionalization.

In order to prove the DNA probe immobilization and target miRNA-DNA hybridization of the PGFET biosensor, Raman spectroscopy was measured in each step (Figure S7). Ag nanoparticles were used to enhance the Raman signals. First, the FAM-labeled DNA probe was introduced on the PLL−graphene surface. In order to eliminate the interference of Ag nanoparticles, the Raman spectrum of PLL−graphene with Ag nanoparticles was first tested (Figure S7a). Figure S7b shows the strong 463, 644, 1168, 1315, 1526, and 1634 cm^{-1} Raman signals of FAM labeled on DNA probes, but there are no FAM signals before the DNA probes loading, indicating that the DNA probes were immobilized on the PLL−graphene surface successfully. To determine the hybridization of target miRNA with a DNA probe, we first immobilize the non-labeled DNA probe on the PLL−graphene surface. Then, the FAM-labeled target miRNAs were loaded and hybridized with the immobilized DNA probes. After the full hybridization between DNA probes and target miRNAs, the microchannel was washed with PBS. To eliminate the interference of DNA probes, first, the Raman spectrum of DNA without FAM labeling was also tested, and no obvious Raman peak of DNA probe was found (Figure S7c). The distinct specific Raman peaks of FAM at 467, 645, 1173, 1316, 1536, and 1633 cm^{-1} appear (Figure S7d (red line)) after target miRNA reaction

https://doi.org/10.1021/acs.analchem.1c03786
Anal. Chem. 2022, 94, 1626−1636

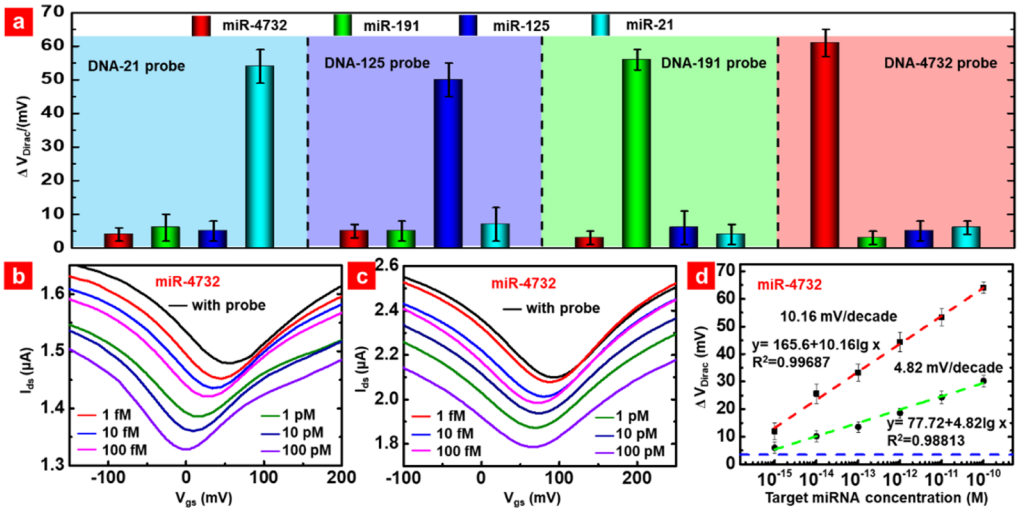

Figure 3. Specificity and sensitivity of the PGFET biosensor. (a) specificity of the PGFET biosensor for 100 pM non-complementary miRNA and complementary miRNA. (b) Transfer characteristics of PGFET biosensor at different miR-4732 concentrations. (c) Transfer characteristics of GFET biosensor at different miR-4732 concentrations. (d) miR-4732 concentrations dependence on ΔV_{dirac} shift and fitted linear equation of the PGFET and GFET biosensors, in which the blue dashed line is the noise level of ~4 mV for the PGFET biosensor.

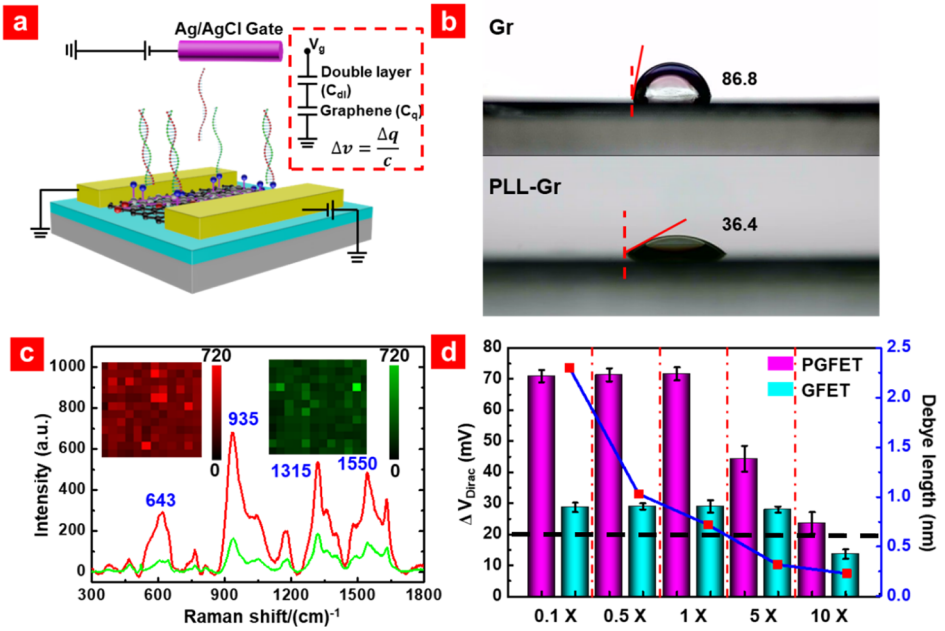

Figure 4. (a) Schematic diagram of PGFET biosensor sensing model. (b) Changes of hydrophilic angle of graphene before and after PLL functionalization of graphene. (c) Raman mapping of miRNA with FAM fluorescent group immobilized on PLL-functionalized Gr (red) and Gr (green). (d) Comparison of the Dirac point offset between PGFET and GFET biosensors at different PBS concentrations, and the theoretical Debye length in different PBS concentrations.

with the DNA probes, while there are no FAM Raman signals shown up by hybridizing FAM-labeled mismatched miRNAs with DNA probes on the PLL−graphene surface [Figure S7d (blue line)], indicating that the DNA probes only hybridize with the target miRNAs.

Detection Process Optimization and PGFET Biosensor Performance. To achieve optimized incubation time between DNA probe in the channel of the PGFET biosensor, a 10 μM probe is loaded into the channel and incubated with different times. The V_{dirac} of the biosensors increases with immobilization time and reaches the maximum value at 5 min, as shown in Figure S8a, which is used as an optimized DNA probe immobilization time. The incubation time of the DNA−miRNA complex in the channel of the biosensors is optimized as shown in Figure S8b. The V_{dirac} of the biosensors DNA−miRNA reaches maximum and a stable status after 10 min. Therefore, DNA−miRNA incubation time is set as 10 min. At the same time, we also optimized the DNA probe immobilization time and SARS-CoV-2 RNA incubation time for SARS-CoV-2 RNA detection, as shown in Figure S8c,d. It also needs 10 min to reach V_{dirac} maximum and a stable status. To verify the specificity of the biosensors, first, the probes related to each of four different breast cancer miRNA biomarkers were immobilized on the channel surface separately; then, 100 pM of miR-4732, miR-191, miR-125, and miR-21 were selected as the targets. Under optimized

https://doi.org/10.1021/acs.analchem.1c03786
Anal. Chem. 2022, 94, 1626−1636

conditions, the V_{dirac} changes of four different breast cancer miRNA biomarkers (miR-21, miR-125, miR-191, and miR-4732) are summarized in Figure 3a. The V_{dirac} shifts of the PGFET biosensors are all less than 10 mV for the non-complementary miRNAs detection, and larger than 50 mV for the complementary miRNAs detection, which gives at least 5-fold differences. The results indicated that the PGFET biosensor delivers excellent specificity between non-target and target miRNAs.

To identify the sensitivity of the PGFET biosensor, different concentrations of complementary miRNAs from 1 fM to 100 pM were tested. From Figure 3b, we can see that the V_{dirac} of the biosensor shifted gradually to the left with the complementary miRNA concentration increasing from 1 fM to 100 pM, which exhibits a 10.16 mV/decade sensitivity with the correlation coefficient $R^2 = 0.99687$ [Figure 3d (red line)]. We have also conducted two repeatability experiments to confirm the detection reproducibility. The average sensitivity is 10.10 mV/decade (Figure S9). The left shift of V_{dirac} indicates that the complementary target miRNA interacts with PGFET biosensors resulting in the n-doping effect of the graphene.[27,46−50] As a comparison, we also tested the sensitivity of GFET biosensors without PLL modification. The sensitivity of the GFET biosensor degraded to 4.76 mV/decade [Figure 3c,d (blue line)], and PLL functionalization realized 113% sensitivity enhancement. At the same time, we also used PGFET biosensors to detect three other breast cancer miRNA biomarkers related to breast cancer, including miR-21, miR-191, and miR-125. As shown in Figure S10, the sensitivities of 10.56, 9.61, and 10.05 mV/decade were achieved, respectively. The slight difference of the sensitivity is probably due to the quality of graphene and processes variation in different devices, which could be solved with success and mature of the single layer graphene growth and device process. The stability of different PGFET biosensors is also tested and shown in Figure S11. The average sensitivity value of PGFET biosensors is 10.05 mV/decade with the standard deviation of 3.97%, proving the relatively stable detection performance of different PGFET biosensors. In addition, we summarized the research progress of GFET biosensors in recent years (Table S1) and found that the developed PGFET biosensor has great advantages in sensitivity, sample consumption volume, and detection time.

Mechanism of the PGFET Biosensor. To study the performance enhancement mechanism of the PGFET biosensors, the electric double layer (EDL) model is established. As shown in Figure 4a, an EDL will be formed at the electrode/electrolyte/graphene interface when a gate voltage V_{gs} is applied. When the molecules (target (mi)RNA) are absorbed on the graphene channel surface, the total gate capacitance (C) of the PGFET biosensor is composed of four parallel plate capacitors (C_{G1}, C_{G2}, C_{G3} and C_Q) connected in series.[25,51]

$$C = \left(\frac{1}{C_{G1}} + \frac{1}{C_{G2}} + \frac{1}{C_{G3}} + \frac{1}{C_Q}\right)^{-1} \quad (1)$$

where C_{G1}, C_{G2}, and C_{G3} represent the capacitance of graphene solution, the (mi)RNA solution, and the reference electrode solution, respectively. C_Q represents the quantum capacitance of graphene associated with the finite density of states due to Pauli's principle.[25,52] The hybridization of DNA-(mi)RNA on the graphene surface of the PGFET biosensor changed the charges (Δq) at the solution−channel surface interface, resulting in the electrostatic potential change in the PGFET biosensor channel; thus, it causes the Dirac point to shift, which follows the relationship

$$\Delta V_{dirac} = \frac{\Delta q}{C} \quad (2)$$

The surface charges change (Δq) could be expressed as $k_a k_b q_a S$, where k_a is the enhancement coefficient of (mi)RNA on graphene surface, k_b is the hybridization efficiency of target (mi)RNA and DNA probe, q_a is the charge contributed by the unit surface density of (mi)RNA adsorbed on the channel surface of the PGFET biosensor, and S is the effective channel area. The eq 2 can be written as

$$\Delta V_{dirac} = \frac{\Delta q}{C} = \frac{k_a k_b q_a S}{C} \quad (3)$$

Therefore, suppose V_{dirac} shift of the PGFET biosensor is $\Delta V_{dirac1} = \frac{k_{a1} k_{b1} q_a S_1}{C_1}$, and V_{dirac} shift of the GFET biosensor is $\Delta V_{dirac2} = \frac{k_{a2} k_{b2} q_a S_2}{C_2}$. Under the same test conditions, the capacitance of the two transistors is basically equal, while the hybridization efficiency of DNA-(mi)RNA is basically unchanged at the same temperature, the same target (mi)RNA concentration and pressure, and the effective channel area of the both biosensors is approximately equal. So

$$\frac{\Delta V_{dirac1}}{\Delta V_{dirac2}} = \frac{\frac{k_{a1} k_{b1} q_a S_1}{C_1}}{\frac{k_{a2} k_{b2} q_a S_2}{C_2}} \approx \frac{k_{a1}}{k_{a2}} \quad (4)$$

k_a represents the enhancement coefficient of miRNA on graphene surface. It means that the performance enhancement of PGFET biosensors could be attributed to the hybridized miRNA enhancement. Here, the Raman spectroscopy was used to verify k_a. First, we studied the changes in the hydrophilic angle of graphene before and after PLL functionalization (Figure 4b). PLL-functionalized graphene reduces the hydrophilic angle to 36.4 from 86.8° of graphene. The decrease in the hydrophilic angle means that the molecules in the solution has a better contact with the graphene, which is conducive to the binding of charged molecules to the surface. To perform the Raman measurement, the DNA probes were fixed on both the PLL-functionalized graphene surface and the bare graphene surface. Then, the target miRNA labeled with FAM was hybridized with the DNA probes for 10 min followed by PBS and DI rinsing to remove unbounded miRNAs. Then, the Raman mappings were measured on the samples. AgNPs were added to enhance the Raman signal. Figure 4c shows a strong FAM Raman signal enhancement on the PLL-functionalized graphene surface (red curve) compared to that on the graphene surface, and better uniformity (inset the mapping). The results indicated that the more miRNAs were hybridized with immobilized DNA probes on the PLL-functionalized graphene surface. To further evaluate enhancement efficiency, we compared the FAM Raman mapping signal intensity quantitatively. In order to avoid the influence of PLL Raman signals, we selected the characteristic peak 1315 cm^{-1} of FAM to represent the distribution of target miRNA. The Raman mapping of FAM-labeled DNA probes is shown in the inset of Figure 4c, in which each point represents one Raman signal intensity of 1315 cm^{-1}. As analyzed above, it should be

https://doi.org/10.1021/acs.analchem.1c03786
Anal. Chem. 2022, 94, 1626−1636

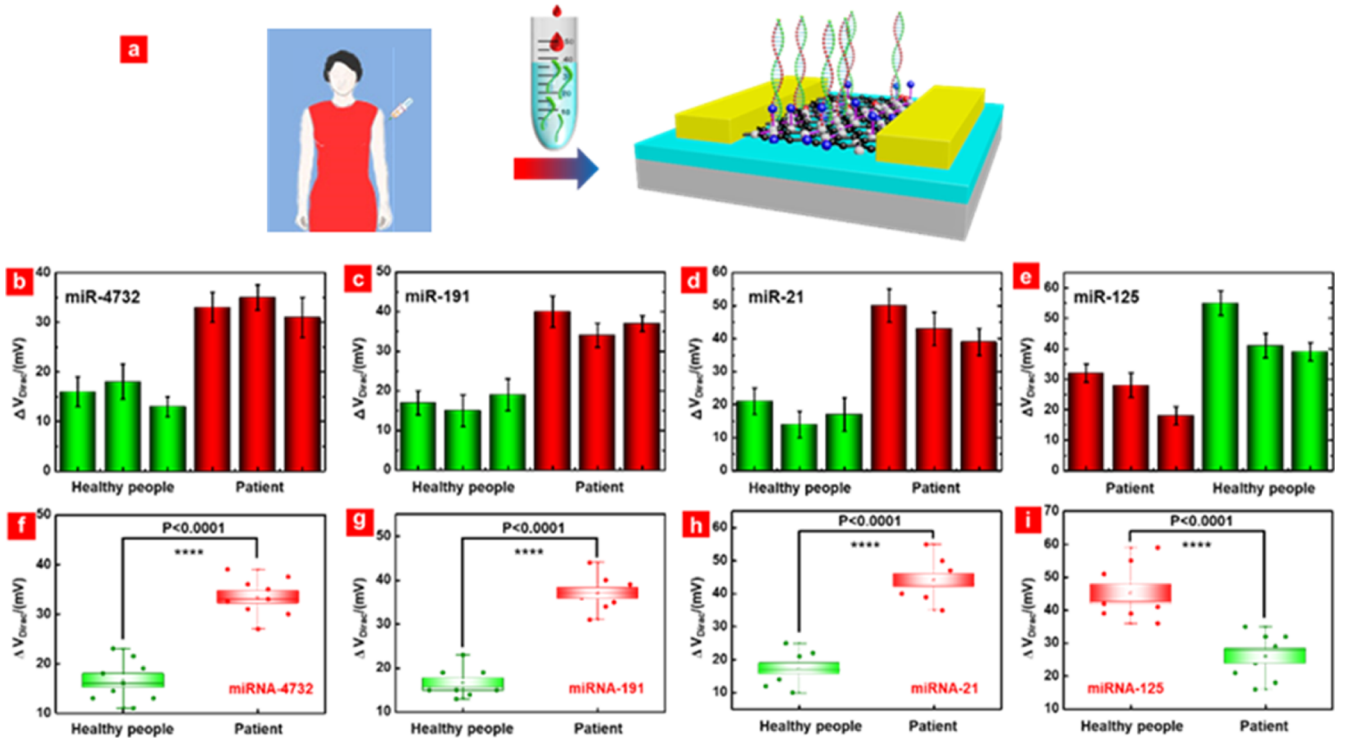

Figure 5. (a) Schematic diagram of miRNA detection process of breast cancer patients. Expression level of miRNA in the serum obtained from healthy and cancer patient samples, (b) miR-4732, (c) miR-191, (d) miR-21, (e) miR-125. Statistical comparison of test results, (f) miR-4732, (g) miR-191, (h) miR-21, (i) miR-125.

$\frac{k_{a1}}{k_{a2}} \propto \frac{h_1}{h_2}$, where h_1 and h_2 are FAM average Raman intensity of 1315 cm^{-1} on the PLL-functionalized graphene and graphene surfaces, respectively. Thus, $\frac{k_{a1}}{k_{a2}} \propto \frac{h_1}{h_2} = 2.9$, which basically equals the sensitivity enhancement factor of 2.11 for PGFET biosensors. Therefore, we can conclude that the functionalization of PLL on the graphene leads to the enhanced adsorption of DNA probes, resulting in target miRNA molecules' hybridization efficiency enhancement, and eventually, triggered a larger Dirac point shift and improved detection sensitivity.

The Debye length is also particularly important for the FET biosensors. So, we studied whether the Debye length is increased after the PLL is functionalized on the graphene surface. After 100 pM target miRNAs were fully hybridized in the channel of the biosensors, the biosensors were tested in different concentrations of PBS solution (concentrations are 0.1×, 0.5×, 1×, 5×, 10×, and the corresponding theoretical Debye length in the PBS solution is shown in Figure 4d (blue line). As the concentration of PBS increases, whether it was a PGFET or GFET biosensor, at low PBS concentration (0.1× to 1×), the Dirac point shift is basically independent on the PBS concentrations, and at high PBS concentrations (5× to 10×), the Dirac point shift decreases with the increase of PBS concentration. Meanwhile, the response signal of the PGFET biosensor is better than that of the GFET biosensor at the same PBS concentration, which exhibits ~3× enhancement at low PBS concentrations from 0.1× to 1×PBS. The phenomenon is incidentally same as the poly (ethylene glycol) (PEG)-functionalized transistor-based biosensor, which also delivered about 3× detectable sensing signal enhancement.[53,54] Gao et al.[55] reasoned that the addition of PEG or other polymer can tune the dielectric properties in the solutions and change the Debye radius of the solution. In our work, we detected the nucleic acid (~0.34 nm/bp in length). As we can see in Figure 4d that 1× PBS solution has a Debye length of ~0.8 nm (blue line), and the DNA−RNA double strand has a width of ~0.68 nm (black dash line), which is in the range of 1× PBS theoretical Debye length. For lower PBS concentration than 1× in PGFET biosensor, the ions in solution have a negligible effect on the target molecule detection. For higher PBS concentration than 1×, the ions in solution would give rise to the negative effect during target molecule detection, resulting in the reduced detection signal. For PGFET biosensors, a PLL-functionalization layer would compensate a little Debye length; therefore, it shows the detectable signal saturation at a little bit lower PBS solution concentration. Eventually, we concluded that the PLL functionalization of the biosensor only enhanced the sensing performance via probe immobilization density enhancement, and would not increase the Debye screening length.

miRNA Detection of Breast Cancer Samples in Serum. Twelve serum samples of breast cancer patients and 12 healthy serum samples were collected as the experimental and the control groups, respectively. They were divided into four groups to test the breast cancer markers miR-4732, miR-191, miR-21, and miR-125 using the PGFET biosensor. The basic detection diagram is shown in Figure 5a. Compared to breast cancer patient serum samples, there is less miRNA expression in normal human serum samples (Figure 5b−e). MiR-125 is a type of down-regulation miRNA, which means that the serum miR-125 level of patients is lower than that of normal people. PGFET biosensors can also distinguish down-regulation miRNA-125, as shown in Figure 5e. The statistical analysis of the real samples test results is shown in Figure 5f−i, which shows a significant difference with $p < 0.0001$ in Student t-test between healthy people and breast cancer patients. Therefore,

https://doi.org/10.1021/acs.analchem.1c03786
Anal. Chem. 2022, 94, 1626−1636

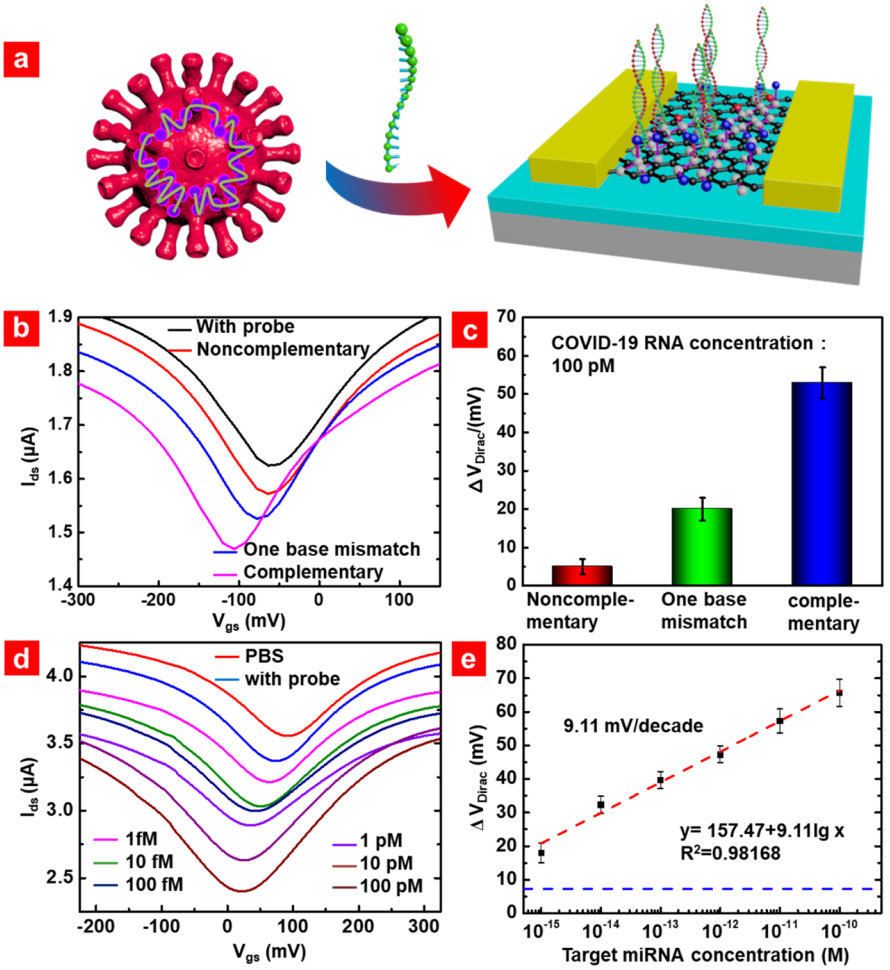

Figure 6. (a) Schematic diagram of SARS-CoV-2 RNA detection process. (b) Transfer characteristics of PGFET biosensor in different samples. (c) V_{dirac} shift values of the PGFET with 100 pM complete mismatch RNA, one base mismatch RNA and target SARS-CoV-2 RNA. (d) SARS-CoV-2 RNA concentrations dependent transfer characteristics of PGFET biosensor. (e) ΔV_{dirac} shifts of the concentration of SARS-CoV-2 RNA corresponding PGFET biosensor.

the results indicated that the developed PGFET biosensor can distinguish the miRNA levels of cancer patients and healthy people, no matter up-regulation or down-regulation miRNA, proving the potential of PGFET biosensors as a distinguishable sensing tool for cancer diagnosis.

Spiked SARS-CoV-2 RNA Detection in Throat Swab Solution. We tried to apply PGFET biosensors to detect SARS-CoV-2 RNA. The schematic diagram of detection process is shown in Figure 6a. The specificity of PGFET biosensors is crucial in the SARS-CoV-2 RNA detection because the SARS-CoV-2 RNA (49 bp) used in the experiments is much longer than that of miRNA. We selected non-complementary SARS-CoV-2 RNA, single base mismatched RNA, and target SARS-CoV-2 RNA to verify the detection specificity of PGFET biosensors. The RNAs were spiked into throat swab solution in order to simulate the SARS-CoV-2 RNA test. Figure 6b shows the transfer characteristic curves of the PGFET after DNA probes immobilization and SARS-CoV-2 RNA hybridization. As shown in Figure 6c, after adding 100 pM non-complementary RNA, the V_{dirac} did not shift obviously; with 100 pM one-base mismatched SARS-CoV-2 RNA, the V_{dirac} shifted ~20 mV to the left; While, V_{dirac} shifted up to ~60 mV to the left with 100 pM SARS-CoV-2 RNA, indicating the good selectivity of the PGFET biosensor for SARS-CoV-2 RNA detection. The sensitivity of SARS-CoV-2 RNA detection is also a key factor for PGFET biosensors. Here, we studied the response of PGFET biosensors to different concentrations of SARS-CoV-2 RNA. Figure 6d shows that as the concentration of SARS-CoV-2 RNA increases from 1 fM to 100 pM, the V_{dirac} of the PGFET biosensor shifted to the left gradually with the SARS-CoV-2 RNA concentration increase. According to the linear fitting of the test results (Figure 6e), the sensitivity of the PGFET biosensor for SARS-CoV-2 RNA detection is 9.11 mV/decade with the correlation coefficient R^2 = 0.98168, which is consistent with miRNA detection results. In practice, there are sensitivity fluctuations in different batch PGFET biosensors, the highest and lowest sensitivity are 9.55 and 8.35 mV/decade with average sensitivity of 9.00 mV/decade, respectively (Figure S12). To further confirm the SARS-CoV-2 RNA detection accuracy of the PGFET biosensor in practical samples, we tested SARS-CoV-2 psuedovirus samples in throat swab solution and compared the detection results with standard qPCR. The SARS-CoV-2 pseudovirus is recombinant pseudotyped lentiviral particles containing a spike protein and gene but without infectivity, which was used for RNA extraction and quality control of detection. As shown in Figures 7 and S13, these two methods correlate well with a

https://doi.org/10.1021/acs.analchem.1c03786
Anal. Chem. 2022, 94, 1626−1636

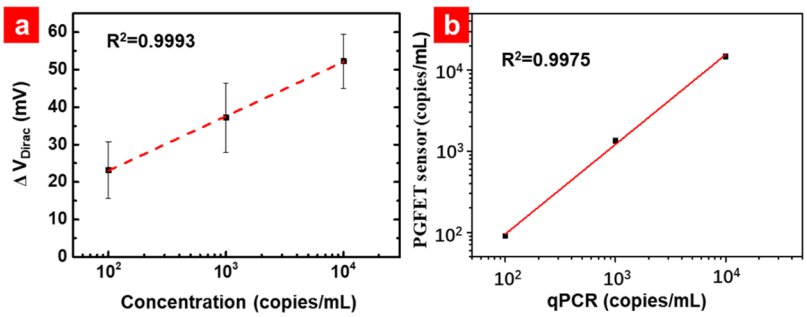

Figure 7. (a) Concentration of SARS-CoV-2 psuedovirus RNA dependent ΔV_{dirac} shifts of the PGFET biosensor. (b) Correlation of PGFET biosensor analysis results with qPCR results for SARS-CoV-2 psuedovirus samples.

slope of ~0.99 (R^2 = 0.9975), which indicated that the detection accuracy of the PGFET biosensor is comparable to that of the qPCR in practical sample analysis. The detection results of spiked SARS-CoV-2 RNA in throat swab solution by PGFET biosensor confirmed the potential application in virus screening, which could be provide a rapid, on-site diagnosis approach of epidemic detection.

CONCLUSIONS

An ultrasensitive biosensor was developed based on the PLL modified graphene FET for rapid, selective, and multifunctional detection of breast cancer miRNA and SARS-CoV-2 RNA. The PGFET biosensor is capable of miRNA and SARS-CoV-2 RNA selective detection with five orders dynamic range and a LOD of as low as 1 fM within 20 min using 2 μL of serum sample, which is more than 113% sensitivity enhancement compared with that of GFET biosensors. The performance enhancement mechanisms of the PGFET biosensor were proposed based on the theoretical model and experimental results, which is attributed to the DNA probe density enhancement promoted by the strong electrostatic force of PLL in the channel of PGFET biosensor. The detection of breast cancer miRNA in human serum and spiked SARS-CoV-2 RNA samples in a human throat swab buffer was performed using PGFET biosensors, proving the potential applications of the PGFET biosensor in disease diagnostics and virus detection.

ASSOCIATED CONTENT

Supporting Information

The Supporting Information is available free of charge at https://pubs.acs.org/doi/10.1021/acs.analchem.1c03786.

Fabrication process of graphene-field effect transistor biosensors; optical microscope image of GFET, AFM image of Gr and PLL- Gr, height profile of graphene, height profile of PLL-Gr; Raman spectrum of PLL; TEM images, diffraction patterns, and EDX images of graphene, PLL/graphene, and DNAprobe/PLL/graphene; before and after PLL functionalization, transfer characteristics of the solution-gated GFET, and transfer characteristics of PGFET; transfer characteristics for typical (a) PGFET and (b) GFET biosensors; Raman spectra of Gr-FET-based biosensors; V_{Dirac} shifts of the GPLL FET dependence on the DNA immobilization, PGFET dependence on the miRNA incubation time, PGFET dependence on the DNA immobilization time, PGFET dependence on the COVID-19 RNA incubation time; properties of PGFET sensors in different fabrication batches, ΔV_{Dirac} dependence of the concentration of target miRNA, transfer characteristics of PGFET, ΔV_{Dirac} dependence of the concentration of target miRNA; transfer characteristics of PGFET biosensors; stability of different PGFET biosensors; transfer characteristics of PGFET biosensor with control sample and SARS-CoV-2 psuedovirus spiked samples; and table of performance and structure of graphene-based solution-gated FET(PDF)

AUTHOR INFORMATION

Corresponding Authors

Yu Zhang − *Institute of Marine Science and Technology, Shandong University, Qingdao 266237, China;* orcid.org/0000-0002-0666-2537; Email: zhang@sdu.edu.cn

Lin Han − *Institute of Marine Science and Technology, Shandong University, Qingdao 266237, China;* orcid.org/0000-0003-0461-2031; Email: hanlin@sdu.edu.cn

Authors

Jianwei Gao − *Institute of Marine Science and Technology, Shandong University, Qingdao 266237, China*

Chunhua Wang − *Institute of Marine Science and Technology, Shandong University, Qingdao 266237, China*

Chao Wang − *Institute of Marine Science and Technology, Shandong University, Qingdao 266237, China*

Yujin Chu − *Institute of Marine Science and Technology, Shandong University, Qingdao 266237, China*

Shun Wang − *Institute of Marine Science and Technology, Shandong University, Qingdao 266237, China*

Ming yuan Sun − *Institute of Marine Science and Technology, Shandong University, Qingdao 266237, China*

Hao Ji − *Institute of Marine Science and Technology, Shandong University, Qingdao 266237, China*

Yakun Gao − *Institute of Marine Science and Technology, Shandong University, Qingdao 266237, China*

Yanhao Wang − *Institute of Marine Science and Technology, Shandong University, Qingdao 266237, China*

Yingkuan Han − *Institute of Marine Science and Technology, Shandong University, Qingdao 266237, China*

Fangteng Song − *Institute of Marine Science and Technology, Shandong University, Qingdao 266237, China*

Hong Liu − *State Key Laboratory of Crystal Materials, Shandong University, Jinan, Shandong 250100, China;* orcid.org/0000-0003-1640-9620

Complete contact information is available at: https://pubs.acs.org/10.1021/acs.analchem.1c03786

https://doi.org/10.1021/acs.analchem.1c03786
Anal. Chem. 2022, 94, 1626−1636

Author Contributions

J.G., Chunhua Wang and Chao Wang contributed equally. Y.Z. and L.H. designed the research, revised the manuscript and provided funds; J.G. conducted the experiment and wrote the manuscript draft; Chao Wang, Y.W., H.J., Y.C., S.W., M.S. and F.S. assisted in the test and completed the experiment; Y.G. provided nucleic acid reagents for the experiment; H.Y. characterized graphene materials; H.L. gave theoretical guidance.

Notes

The authors declare no competing financial interest.

■ ACKNOWLEDGMENTS

This work was supported by the National Key R&D Plan of China (grant no. 2017YFB0405400), Natural Science Foundation for Distinguished Young Scientist of Shandong Province (grant no. JQ201814), State Key Laboratory of Microbial Technology Open Projects Fund (project nos. M2021-01 and M2021-07), Shandong University multidisciplinary research and innovation team of young scholars, and Collaborative Innovation Center of Technology and Equipment for Biological Diagnosis and Therapy in Universities of Shandong, Collaborative Innovation Center of Technology and Equipment for Biological Diagnosis and Therapy in Universities of Shandong. The authors would like to thank Haiyan Yu, Xiaomin Zhao, Sen Wang, and Yuyu Guo from the State Key laboratory of Microbial Technology of Shandong University for help and guidance in material characterization.

■ REFERENCES

(1) Gebert, L. F. R.; MacRae, I. J. *Nat. Rev. Mol. Cell Biol.* **2019**, *20*, 21−37.
(2) Hurtley, S. M. *Science* **2020**, *370*, 48.
(3) Kim, Y.; Kim, H.; Bang, S.; Jee, S.; Jang, K. *Lab. Invest.* **2021**, *101*, 155−164.
(4) Dave, V. P.; Ngo, T. A.; Pernestig, A.-K.; Tilevik, D.; Kant, K.; Nguyen, T.; Wolff, A.; Bang, D. D. *Lab. Invest.* **2019**, *99*, 452−469.
(5) Rupaimoole, R.; Slack, F. J. *Nat. Rev. Drug Discovery* **2017**, *16*, 203−222.
(6) Asakura, K.; Kadota, T.; Matsuzaki, J.; Yoshida, Y.; Yamamoto, Y.; Nakagawa, K.; Takizawa, S.; Aoki, Y.; Nakamura, E.; Miura, J.; Sakamoto, H.; Kato, K.; Watanabe, S.-i.; Ochiya, T. *Commun. Biol.* **2020**, *3*, 134.
(7) McGeary, S. E.; Lin, K. S.; Shi, C. Y.; Pham, T. M.; Bisaria, N.; Kelley, G. M.; Bartel, D. P. *Science* **2019**, *366*, No. eaav1741.
(8) Tian, T.; Wang, J.; Zhou, X. *Org. Biomol. Chem.* **2015**, *13*, 2226−2238.
(9) Fan, L.; Chong, X.; Zhao, M.; Jia, F.; Wang, Z.; Zhou, Y.; Lu, X.; Huang, Q.; Li, P.; Yang, Y.; Hu, Z.; Li, Q.; Zhang, X.; Shen, L. *Anal. Chem.* **2021**, *93*, 665−670.
(10) Ter-Ovanesyan, D.; Gilboa, T.; Lazarovits, R.; Rosenthal, A.; Yu, X.; Li, J. Z.; Church, G. M.; Walt, D. R. *Anal. Chem.* **2021**, *93*, 5365−5370.
(11) Zhong, G.-X.; Ye, C.-L.; Wei, H.-X.; Yang, L.-Y.; Wei, Q.-X.; Liu, Z.-J.; Fu, L.-X.; Lin, X.-H.; Chen, J.-Y. *Anal. Chem.* **2021**, *93*, 911−919.
(12) Schwierz, F. *Nat. Nanotechnol.* **2010**, *5*, 487−496.
(13) Park, J. M.; Cao, Y.; Watanabe, K.; Taniguchi, T.; Jarillo-Herrero, P. *Nature* **2021**, *590*, 249−255.
(14) Gobbi, M.; Galanti, A.; Stoeckel, M.-A.; Zyska, B.; Bonacchi, S.; Hecht, S.; Samorì, P. *Nat. Commun.* **2020**, *11*, 4731.
(15) Sakata, T.; Nishitani, S.; Saito, A.; Fukasawa, Y. *ACS Appl. Mater. Interfaces* **2021**, *13*, 38569−38578.
(16) Fathi-Hafshejani, P.; Azam, N.; Wang, L.; Kuroda, M. A.; Hamilton, M. C.; Hasim, S.; Mahjouri-Samani, M. *ACS Nano* **2021**, *15*, 11461−11469.
(17) Shao, W.; Shurin, M. R.; Wheeler, S. E.; He, X.; Star, A. *ACS Appl. Mater. Interfaces* **2021**, *13*, 10321−10327.
(18) Yu, Y.; Li, Y.-T.; Jin, D.; Yang, F.; Wu, D.; Xiao, M.-M.; Zhang, H.; Zhang, Z.-Y.; Zhang, G.-J. *Anal. Chem.* **2019**, *91*, 10679−10686.
(19) Kanai, Y.; Ohmuro-Matsuyama, Y.; Tanioku, M.; Ushiba, S.; Ono, T.; Inoue, K.; Kitaguchi, T.; Kimura, M.; Ueda, H.; Matsumoto, K. *ACS Sens.* **2020**, *5*, 24−28.
(20) Xu, S.; Wang, T.; Liu, G.; Cao, Z.; Frank, L. A.; Jiang, S.; Zhang, C.; Li, Z.; Krasitskaya, V. V.; Li, Q.; Sha, Y.; Zhang, X.; Liu, H.; Wang, J. *Sens. Actuators, B* **2021**, *326*, 128991.
(21) Wu, D.; Yu, Y.; Jin, D.; Xiao, M.-M.; Zhang, Z.-Y.; Zhang, G.-J. *Anal. Chem.* **2020**, *92*, 4006−4015.
(22) Gao, J.; Gao, Y.; Han, Y.; Pang, J.; Wang, C.; Wang, Y.; Liu, H.; Zhang, Y.; Han, L. *ACS Appl. Electron. Mater.* **2020**, *2*, 1090−1098.
(23) Li, S.; Huang, K.; Fan, Q.; Yang, S.; Shen, T.; Mei, T.; Wang, J.; Wang, X.; Chang, G.; Li, J. *Biosens. Bioelectron.* **2019**, *136*, 91−96.
(24) Xu, S.; Jiang, S.; Zhang, C.; Yue, W.; Zou, Y.; Wang, G.; Liu, H.; Zhang, X.; Li, M.; Zhu, Z.; Wang, J. *Appl. Surf. Sci.* **2018**, *427*, 1114−1119.
(25) Xu, S.; Zhan, J.; Man, B.; Jiang, S.; Yue, W.; Gao, S.; Guo, C.; Liu, H.; Li, Z.; Wang, J.; Zhou, Y. *Nat. Commun.* **2017**, *8*, 14902.
(26) Wang, Z.; Hu, S.; Li, F.; Fan, Q.; Jia, Y. *Analyst* **2019**, *144*, 4787−4794.
(27) Cai, B.; Huang, L.; Zhang, H.; Sun, Z.; Zhang, Z.; Zhang, G.-J. *Biosens. Bioelectron.* **2015**, *74*, 329−334.
(28) Zheng, C.; Huang, L.; Zhang, H.; Sun, Z.; Zhang, Z.; Zhang, G.-J. *ACS Appl. Mater. Interfaces* **2015**, *7*, 16953−16959.
(29) Seo, G.; Lee, G.; Kim, M. J.; Baek, S.-H.; Choi, M.; Ku, K. B.; Lee, C.-S.; Jun, S.; Park, D.; Kim, H. G.; Kim, S.-J.; Lee, J.-O.; Kim, B. T.; Park, E. C.; Kim, S. I. *ACS Nano* **2020**, *14*, 5135−5142.
(30) Chu, Y.; Gao, Y.; Tang, W.; Qiang, L.; Han, Y.; Gao, J.; Zhang, Y.; Liu, H.; Han, L. *Anal. Chem.* **2021**, *93*, 5129−5136.
(31) Gao, Y.; Han, Y.; Wang, C.; Qiang, L.; Gao, J.; Wang, Y.; Liu, H.; Han, L.; Zhang, Y. *Anal. Chim. Acta* **2021**, *1154*, 338330.
(32) Han, Y.; Qiang, L.; Gao, Y.; Gao, J.; He, Q.; Liu, H.; Han, L.; Zhang, Y. *Appl. Surf. Sci.* **2021**, *541*, 148456.
(33) Song, F.; Wang, C.; Wang, C.; Gao, J.; Liu, H.; Zhang, Y.; Han, L. *Anal. Chem.* **2021**, *93*, 4697−4706.
(34) Pang, J.; Bachmatiuk, A.; Fu, L.; Yan, C.; Zeng, M.; Wang, J.; Trzebicka, B.; Gemming, T.; Eckert, J.; Rummeli, M. H. *J. Phys. Chem. C* **2015**, *119*, 13363−13368.
(35) Kim, S.; Kwak, D. H.; Choi, I.; Hwang, J.; Kwon, B.; Lee, E.; Ye, J.; Lim, H.; Cho, K.; Chung, H.-J.; Lee, W. H. *ACS Appl. Mater. Interfaces* **2020**, *12*, 55493−55500.
(36) Nagamura, N.; Fukidome, H.; Nagashio, K.; Horiba, K.; Ide, T.; Funakubo, K.; Tashima, K.; Toriumi, A.; Suemitsu, M.; Horn, K.; Oshima, M. *Carbon* **2019**, *152*, 680−687.
(37) Wang, C.; Wang, C.; Qiu, J.; Gao, J.; Liu, H.; Zhang, Y.; Han, L. *Microchim. Acta* **2021**, *188*, 262.
(38) Wang, C.; Zhang, Y.; Tang, W.; Wang, C.; Han, Y.; Qiang, L.; Gao, J.; Liu, H.; Han, L. *Anal. Chim. Acta* **2021**, *1178*, 338791.
(39) Korzeniewski, C.; Kitt, J. P.; Bukola, S.; Creager, S. E.; Minteer, S. D.; Harris, J. M. *Anal. Chem.* **2019**, *91*, 1049−1055.
(40) Arihori, K.; Ogawa, M.; Souma, S.; Sato-Iwanaga, J.; Suzuki, M.-a. *J. Appl. Phys.* **2021**, *130*, 084302.
(41) Gorman, A.; Hossain, K. R.; Cornelius, F.; Clarke, R. J. *Biochim. Biophys. Acta, Biomembr.* **2020**, *1862*, 183128.
(42) Gao, J.; Wang, Y.; Han, Y.; Gao, Y.; Wang, C.; Han, L.; Zhang, Y. *J. Mater. Sci.: Mater. Electron.* **2020**, *31*, 15372−15380.
(43) Ramadan, S.; Lobo, R.; Zhang, Y.; Xu, L.; Shaforost, O.; Kwong Hong Tsang, D.; Feng, J.; Yin, T.; Qiao, M.; Rajeshirke, A.; Jiao, L. R.; Petrov, P. K.; Dunlop, I. E.; Titirici, M.-M.; Klein, N. *ACS Appl. Mater. Interfaces* **2021**, *13*, 7854−7864.
(44) Li, Y.; Peng, Z.; Holl, N. J.; Hassan, M. R.; Pappas, J. M.; Wei, C.; Izadi, O. H.; Wang, Y.; Dong, X.; Wang, C.; Huang, Y.-W.; Kim, D.; Wu, C. *ACS Omega* **2021**, *6*, 6643−6653.

https://doi.org/10.1021/acs.analchem.1c03786
Anal. Chem. 2022, 94, 1626−1636

(45) Wang, R.; Mao, Y.; Wang, L.; Qu, H.; Chen, Y.; Zheng, L. *Food Chem.* **2021**, *347*, 128980.
(46) Tian, M.; Qiao, M.; Shen, C.; Meng, F.; Frank, L. A.; Krasitskaya, V. V.; Wang, T.; Zhang, X.; Song, R.; Li, Y.; Liu, J.; Xu, S.; Wang, J. *Appl. Surf. Sci.* **2020**, *527*, 146839.
(47) Srivastava, A. K.; Dwivedi, N.; Dhand, C.; Khan, R.; Sathish, N.; Gupta, M. K.; Kumar, R.; Kumar, S. *Mater. Today Chem.* **2020**, *18*, 100385.
(48) Hwang, M. T.; Heiranian, M.; Kim, Y.; You, S.; Leem, J.; Taqieddin, A.; Faramarzi, V.; Jing, Y.; Park, I.; van der Zande, A. M.; Nam, S.; Aluru, N. R.; Bashir, R. *Nat. Commun.* **2020**, *11*, 1543.
(49) Lopez, A.; Liu, J. *Adv. Intell. Syst.* **2020**, *2*, 2000123.
(50) Chen, S.; Sun, Y.; Xia, Y.; Lv, K.; Man, B.; Yang, C. *Biosens. Bioelectron.* **2020**, *156*, 112128.
(51) Mir, A.; Abhilesh, G. N.; Tamgadge, R. M.; Shukla, A. *J. Solid State Electrochem.* **2019**, *23*, 2281−2290.
(52) Cao, Y.; Park, J. M.; Watanabe, K.; Taniguchi, T.; Jarillo-Herrero, P. *Nature* **2021**, *595*, 526−531.
(53) Chakkarapani, S. K.; Lee, S.; Park, B.; Seo, H.-Y.; Kang, S. H. *ACS Sens.* **2019**, *4*, 953−960.
(54) Assen, A. H.; Yassine, O.; Shekhah, O.; Eddaoudi, M.; Salama, K. N. *ACS Sens.* **2017**, *2*, 1294−1301.
(55) Gao, N.; Zhou, W.; Jiang, X.; Hong, G.; Fu, T.-M.; Lieber, C. M. *Nano Lett.* **2015**, *15*, 2143−2148.

https://doi.org/10.1021/acs.analchem.1c03786
Anal. Chem. 2022, 94, 1626−1636